Geophysical Journal International

Geophys. J. Int. (2017) **210,** 594–608
Advance Access publication 2017 May 1
GJI Seismology

doi: 10.1093/gji/ggx180

Improving the characterization of the seismic source in Bebedouro, Paraná Basin, Brazil: further evidence of seismicity triggered by hydraulic stimulation in water wells

Gabriel Dicelis,[1] Marcelo Assumpção,[1] Renato Luiz Prado,[1] Hans Agurto-Detzel[1,2] and José Roberto Barbosa[1]

[1] *Geophysics Department, University of São Paulo, Rua do Matão* 1226, 05508-090, *Brazil. E-mail: gdicelis@alumni.usp.br*
[2] *Université Côte d'Azur, IRD, CNRS, OCA, Géoazur,* 250 *rue Albert Einstein, F*-06560 *Valbonne, France*

Accepted 2017 April 28. Received 2017 April 26; in original form 2016 September 12

SUMMARY

We investigate a long series of small earthquakes (magnitude < 3) with annual cycles between 2004 and 2010 that occurred in the northeastern Paraná Basin, Brazil. These events were attributed to pore pressure increase in a fractured aquifer caused by the drilling of several water wells down to depths of ∼200 m. Because of the poor depth constraints of the initial study, we relocated ∼1000 microtremors recorded by the local seismographic network using a more accurate velocity model. To better relocate the events, we based the velocity model on geophysical survey data obtained using several techniques, including seismic refraction, surface wave dispersion, vertical electrical sounding, high-frequency receiver functions and the time-domain electromagnetic method. The best 1-D model was calibrated using a simultaneous inversion of hypocentres and a velocity model including station corrections. The resulting focal depths, which are mostly between 100 and 175 m, place the events at depths consistent with the confined aquifer within the basaltic pack. This result confirms that the earthquakes are related to geological stress disturbances (pore pressures) in pre-existing fracture zones within the basalt layer caused by the perforation of water wells used for irrigation. We used a combination of cross-correlations and arrival times to analyse a cluster of 19 earthquakes. The improved hypocentre distribution of this cluster allowed the determination of a clear fault-plane solution, which indicates a normal fault striking WNW-ESE and dipping to the north, with an NNE-SSW extension (*T*-axis). This mechanism complements stress data collected in southeastern Brazil and is consistent with the regional stress regime.

Key words: Hydrogeophysics; South America; Induced seismicity; Seismicity and tectonics; Intra-plate processes.

1 INTRODUCTION

Among several studies of water transfer (e.g. reservoir impoundment, hydraulic fracturing, fluid injection and extraction, mining and exploiting aquifers below rock layers), there is a consensus regarding the principal mechanism that causes the associated induced earthquakes: changes in the stress conditions along faults facilitate failure. This mechanism, initially proposed by Hubbert & Rubey (1959), suggests that the rise in the pore pressures within nearby fault zones lowers the effective stress and frictional resistance on faults, eventually producing earthquakes. In addition, structural or lithologic inhomogeneities can produce conditions that locally amplify the stress conditions on the affected faults; these inhomogeneities involve temperature, rock strength, the orientations of pre-existing faults relative to the local stress field and reservoir permeability (Simpson & Narasimhan 1990; McGarr *et al.* 2002; Shapiro & Dinske 2009; Zoback 2012; Rubinstein & Mahani 2015).

Raleigh *et al.* (1976) were the first to demonstrate that fluid pressure may control the rate of earthquake occurrence by adjusting pore pressure at depth. Since this research, many examples of induced earthquakes and earthquake sequences have been identified, although most of these studies have focused on earthquakes induced by deep injections of fluids at high pressures (Ellsworth 2013). Some of the most notable examples include earthquakes in Ohio, USA (Seeber *et al.* 2004; Kim 2013); Texas, USA (Davis *et al.* 1995; Frohlich 2012); Arkansas, USA (Cox 1991; Horton 2012); Oklahoma, USA (Holland 2013; Keranen *et al.* 2014; Sumy *et al.* 2014); the enhanced geothermal system in Basel, Switzerland (Deichmann & Giardini 2009); and even the extraction of natural gas from shallow deposits in the Netherlands (Eck *et al.* 2006).

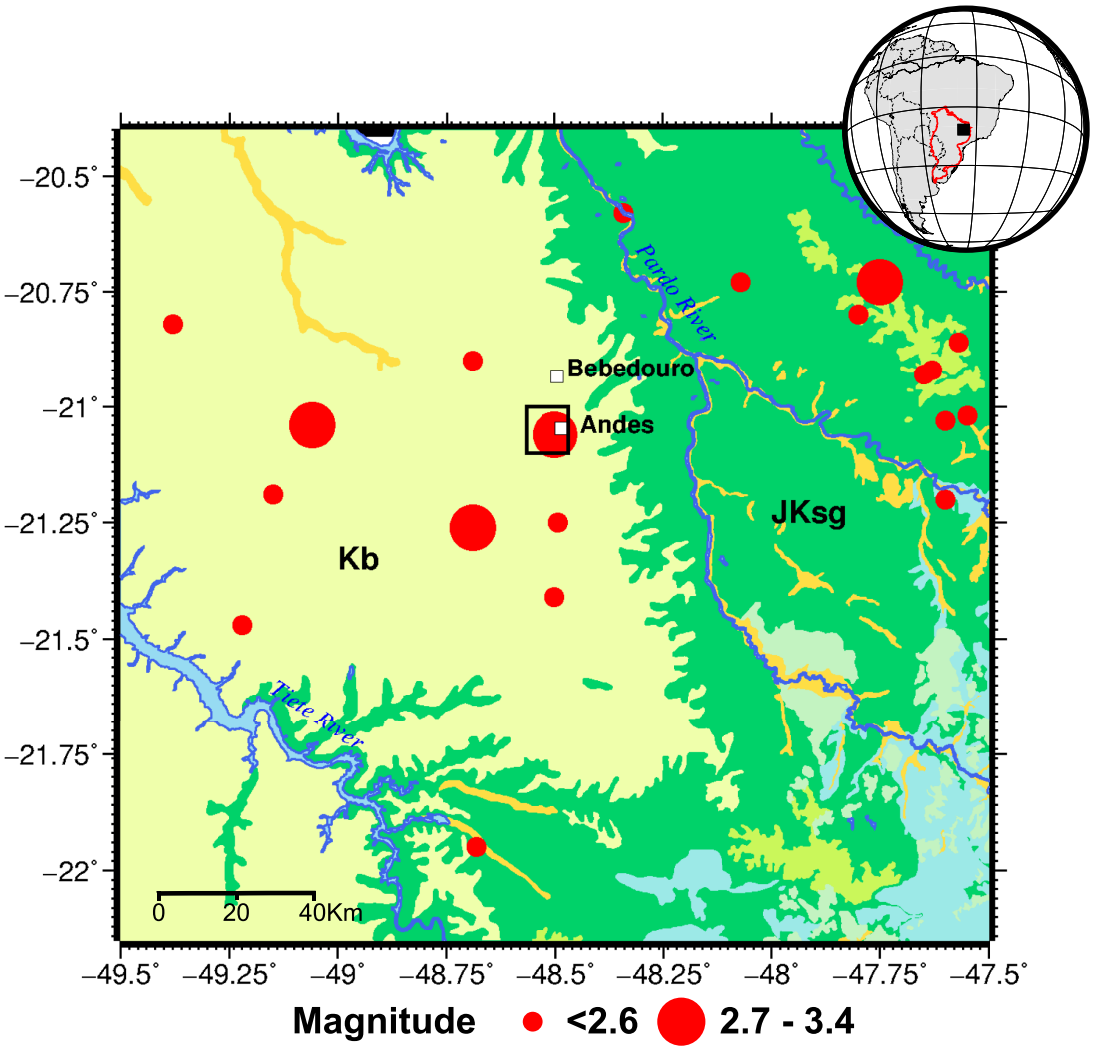

Figure 1. Location, regional geology and past seismicity in the northeastern Paraná Basin (2001–2014). The light yellow (Kb) denotes the Upper Cretaceous sandstones and green (JKsg) denotes the underlying Lower Cretaceous basalts. The geology from the CPRM (Geological Survey of Brazil). The red circles are the epicentres from the Brazilian earthquake catalogue (Assumpção *et al.* 2014). The inset map of Brazil shows the boundary of the Paraná Basin (red line) and the boundaries of Fig. 1 (black solid box). The black box displays the boundaries of the seismicity map presented in Fig. 3.

However, there are also examples in which wells that inject water without added pressure can increase the fluid pressure within rock formations, thereby potentially inducing earthquakes (e.g. Rubinstein & Mahani 2015). For example, the majority of the wells in the Raton Basin, USA, inject water using only gravity and have induced an earthquake sequence that has been ongoing since 2001 and includes earthquakes of $M > 5$ (Barnhart *et al.* 2014; Rubinstein *et al.* 2014).

In early 2004, a series of small earthquakes alarmed the local population of the Andes District, Bebedouroand SE Brazil (Fig. 1). Shortly afterwards, a local seismographic network was deployed, and it recorded more than 5000 micro-earthquakes from 2005 until 2009 (Assumpção *et al.* 2010). This seismic activity, with magnitudes as large as 2.9 and Modified Mercalli intensities of V, occurred near water wells (120–200 m deep) that had been drilled in early 2003 for irrigation purposes. In a previous study, Assumpção *et al.* (2010) showed that (1) the water wells allowed water transfer by gravity from an upper aquifer located in the sandstone layer to a lower aquifer located in the fractured basalt pack; (2) the lower aquifer is progressively charged with water during the rainy season and (3) the spatiotemporal evolution of the seismicity strongly suggested that it was related to the operation of the water wells.

The seismic activity occurred as clustered events with annual cycles, mostly after the rainy season. When the wells were pumped for irrigation, no earthquakes occurred (Fig. 2), possibly because the pumping lowered the water table, reduced pore pressure and thereby strengthened the faults and suppressed earthquakes. Based on the cross-correlation, the time phase shift between the rainfall and earthquakes was estimated to be approximately two months. The seismic diffusivities calculated by Assumpção *et al.* (2010) were mostly in the range 0.1–1 $m^2\ s^{-1}$, consistent with the expected range for reservoir-induced and water-injection seismicity (Shapiro *et al.* 1997, 2002).

In Bebedouro, no clear correlation has been found between the confined aquifer within the basalt pack and the depth of the microseismicity. This lack of correlation was attributed to hypocentral uncertainties (Assumpção *et al.* 2010). Thus, improving hypocentre accuracy is of vital importance for understanding the mechanism responsible for the seismicity. Beginning in 2005, several geophysical

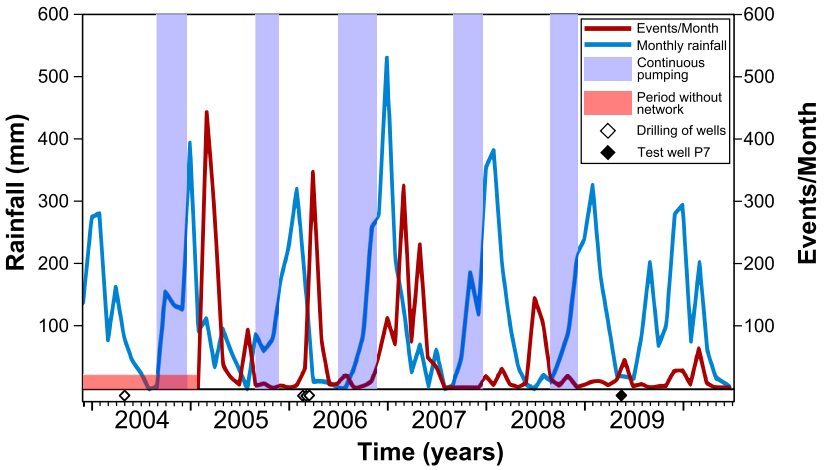

Figure 2. Annual evolution of seismic activity (red line), monthly rainfall (blue line), drilling (open diamonds) and continuous pumping (violet bars) during the dry season. The red line shows the number of earthquakes detected by the seismic network each month, with magnitudes ranging from ~0 to 2.9. Note the striking correlation between the seismic activity and periods without pumping. The red horizontal bar denotes the period when the earthquakes were felt before the deployment of the seismic network. The solid diamond in 2009 denotes a pumping test in well P7. This figure is based on data published by Assumpção *et al*. (2010).

surveys were performed in the Bebedouro area. The geophysical techniques included shallow seismic refraction, high-frequency receiver functions, surface wave dispersion, vertical electrical sounding (VES) and the time-domain electromagnetic method (TDEM). The goal of these studies was to understand the causes of the seismic activity and to develop a more accurate local velocity model (understood as the variations in seismic *P*- and *S*-wave velocity structures), which could improve the hypocentral estimations in this area. We tested various absolute location algorithms for the joint and relative location techniques taken from the available literature: HYPO71

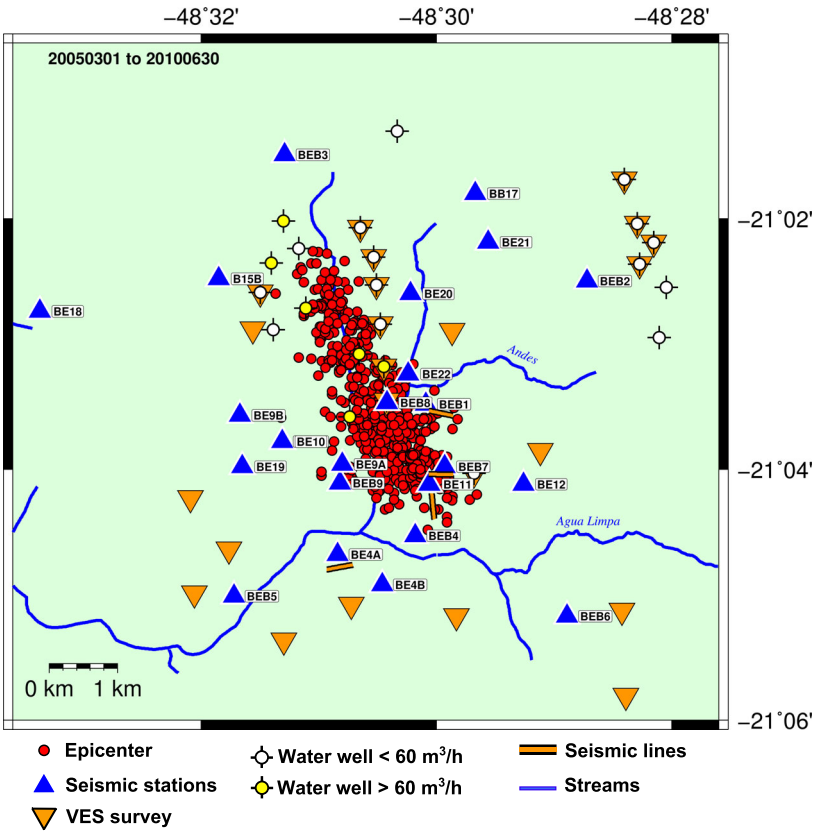

Figure 3. Distribution of seismic network and initial earthquake locations. The red circles represent the preliminary estimated epicentres of the ~3000 earthquakes recorded from 2005 March to 2010 July. The blue triangles are the seismic stations, orange triangles are VES surveys and white and yellow circles are the deep-water wells with flow capacities of less and greater than 60 m^3 hr^{-1}, respectively. The seismic refraction lines are represented by orange dashed lines. Seismic stations were moved around during the five years, with up to eight operating simultaneously.

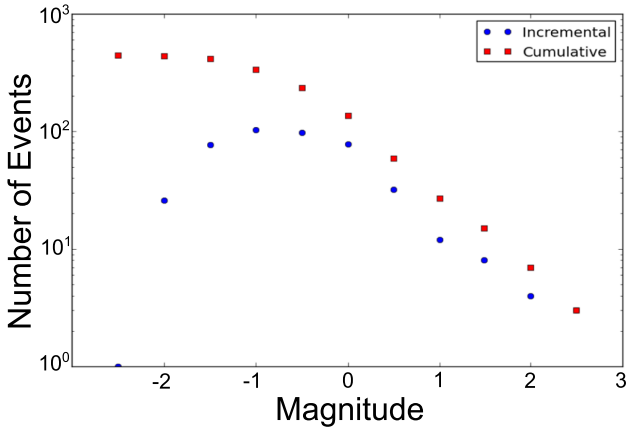

Figure 4. Frequency–magnitude distribution. The number of earthquakes in magnitude bins of 0.5 units. The blue circles and red squares are the incremental and cumulative frequencies, respectively. The *b*-value is 0.68 ± 0.05, for a completeness magnitude of $Mc = 0$.

(Lee & Lahr 1975), HYPOCENTRE (Lienert *et al.* 1986; Lienert & Havskov 1995), VELEST (Kissling *et al.* 1994), the SEISAN software package (Havskov & Ottemöller 1999) and the HypoDD2 code (Waldhauser & Ellsworth 2000; Waldhauser 2001). Our simultaneous inverse modelling produced a substantial improvement in the final 1-D model, allowing us to obtain accurate and reliable locations of the microtremors. The resulting depths confirm the induced nature of the seismicity and indicate that the earthquakes were related to geological stress disturbances (pore pressures) in pre-existing fracture zones within the basalt layer.

In addition, we defined the fault plane of a representative cluster of events by computing their relative locations and a composite focal mechanism.

2 LOCATION AND GEOLOGY

Our study area is located in the northeastern Paraná Basin, Brazil, which is a large intracratonic basin that is elongated NNE-SSW (1750 km long and 900 km wide; see Fig. 1). Ar–Ar ages determined by Turner *et al*. (1994) in the Paraná Basin indicate that, from 138 to 127 Ma, volcanism associated with the separation of the South American continent from Africa released lava flows with a total thickness of as much as 1.5 km that covered the Botucatu desert sediments. This volcanism resulted in a sequence of basalt layers that now traps several fractured aquifers (Milani 2004). The layered basalt pack also confines the present Guarani aquifer, located in the underlying Botucatu sediments. After the lava flows were deposited, a new calciferous sandstone sequence with an average thickness of 150 m was deposited; this sandstone formed the Bauru Basin sedimentary rocks and the Bauru surface aquifer (Milani *et al.* 2007).

Bebedouro lies at the edge of a seismic zone (with many natural low-magnitude earthquakes) that includes the southern Minas Gerais state, the Minas Triangle and the northeastern region of the São Paulo state (Berrocal *et al.* 1984; Assumpção *et al.* 2004; Assumpção & Sacek 2013, Fig. 1). In Bebedouro, the wells cross a sandstone layer approximately 50–120 m thick and extract water from a confined aquifer located below in a fractured zone within the basalt-flow layers. The average thickness of the basalt pack in this region is approximately 500 m. The confined aquifer was known to be shallower than 200 m and most shallow wells (Upper Bauru aquifer) penetrate only the upper sedimentary layer, producing low flows (<10 m^3 hr^{-1}), whereas the wells that reach the lower fractured aquifer in the upper part of the basalt pack produce large flows and are used primarily for irrigation. The out flow varies greatly; most wells produce flows of 20–30 m^3 hr^{-1}, but some reach 150–190 m^3 hr^{-1} (Assumpção *et al.* 2010).

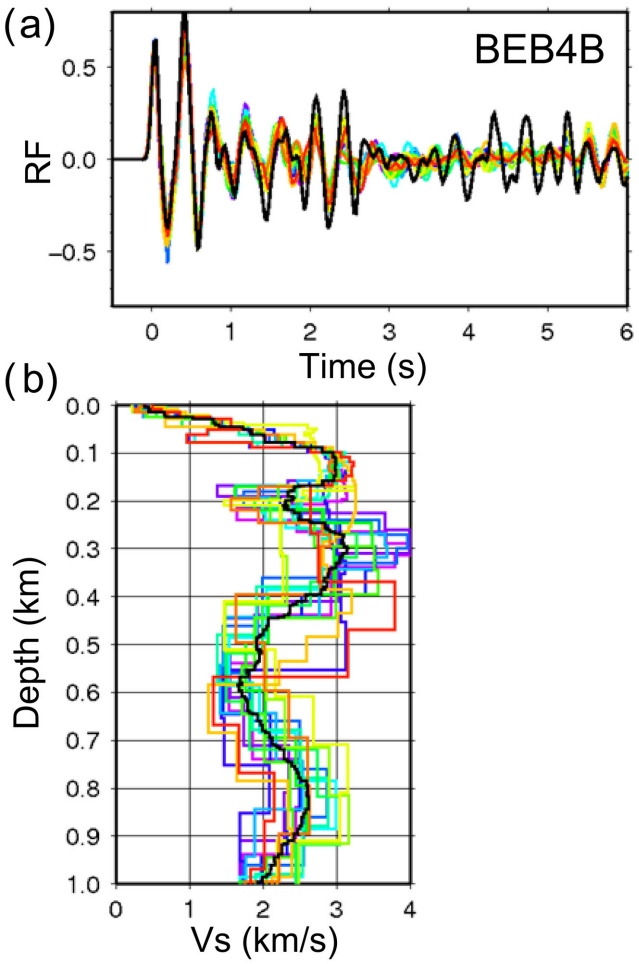

Figure 5. High-frequency receiver function (RF) at station BEB4B. (a) The observed RF (black trace) and coloured traces are good-fitting synthetics. (b) The inverted models coloured according to the goodness of fit (red = best fit). The black trace is the average for all good-fitting models.

3 INITIAL EARTHQUAKE LOCATIONS

From 2005 March to 2010 August, we deployed a network consisting of as many as eight simultaneous three-component short-period seismic stations and three broad-band seismic stations (Fig. 3). Data were recorded at a sampling rate of 100–200 Hz in the trigger mode. The arrival times of the *P* (longitudinal) and *S* (transverse) waves were manually picked from 3113 events (17 831 *P* and 10 105 *S* arrivals) and were assigned weightings based on their quality (signal/noise ratio, sampling frequencies, distance to stations and three-component records). Due to the small amount of available information for the area, the preliminary hypocentres were obtained with HYPO71, using a simple two-layer model of sandstone and basalt, consisting of *P* velocities of 2.2 km s^{-1} in the upper 70 m thick sandstone layer and 5.4 km s^{-1} in the basalt pack, based on existing geological information and a few preliminary tests. An average *Vp*/*Vs* ratio of 1.80 was applied to all layers, based on a Wadati diagram.

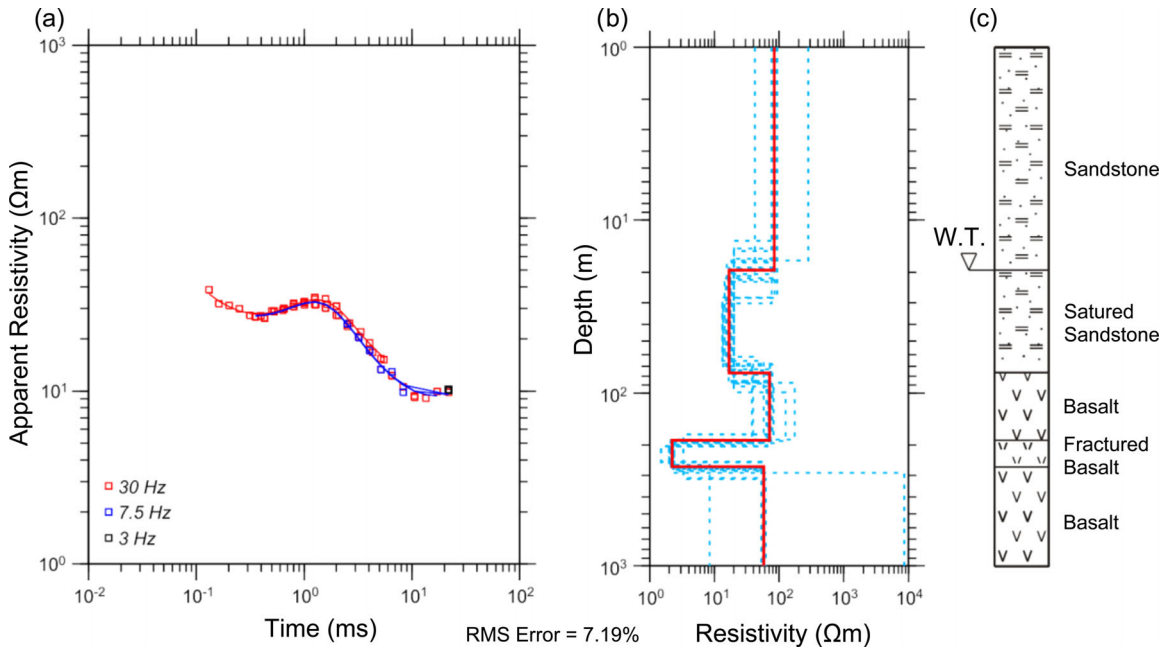

Figure 6. Data from the TDEM survey and preliminary 1-D interpretation. (a) Apparent resistivities: the three colours are samples from different repetition frequencies: 30 Hz for measuring shorter decays (red) and 7.5–3 Hz for measuring longer decay times (light and dark blue, respectively). (b) 1-D inversion: the red line is the best solution; the dashed lines are the range of possible solutions. (c) Geological interpretation: W.T. is the water table. The basalt pack in this region is an average of ∼500 m thick.

Additionally, station corrections were used to compensate for the different sandstone thicknesses. Using this preliminary model, Assumpção *et al*. (2010) concluded that the epicentres extended across an area measuring approximately 5 km long and 1.5 km wide (Fig. 3). The location errors were approximately 200 m for the epicentres and 200−1000 m for the hypocentral depths. This large depth uncertainty makes it difficult to verify that the micro-earthquakes originated within the basalt pack, which is expected to be ∼500 m thick.

Fig. 4 shows the distribution of the earthquake magnitudes in Bebedouro. These local magnitudes were estimated from the relationship between the regional magnitudes m_R (Assumpção 1983) for the stronger events recorded at regional distances and the signal duration measured by the coda waves (trailing, scattered waves after the direct *S* wave) at the local network. Fig. 4(b) shows the cumulative number of events (*Nc*) for each magnitude bin for a set of 724 events in Bebedouro (Oliveira *et al.* 2014). Above a completeness magnitude of $Mc = 0.0$ (i.e. the magnitude above which all events are recorded by the local network), it can be seen that the cumulative number of events follows the classical Gutenberg–Richter frequency–magnitude relationship (eq. 1):

$$\log_{10} Nc = a - bM \quad (1)$$

where *a* and *b* are constants (Gutenberg & Richter 1942). The *a*-value indicates the total seismicity rate of the region. The *b* parameter or *b*-value is the slope of the exponential distribution and relates the number or rate of small to large earthquakes. Several studies have used *b*-value as an indirect indicator of the changes of the stress within fault systems (Wiemer & Wyss 2000; Schorlemmer *et al.* 2005; Farrell *et al.* 2009; Bachman *et al.* 2012). Over a long period and across large areas of active tectonics, *b* tends to be near 1, whereas volcanic systems and induced-seismicity sequences are generally characterized by a *b*-value greater than 1.0 (Schorlemmer *et al.* 2005; Bachmann *et al.* 2011).

We found that the *b*-value for the whole catalogue (Fig. 4) was 0.7. The low *b*-value is a not usual for induced seismicity. However, in relation to hydraulic fracturing sequences, some authors suggest that higher *b*-values are associated with micro-earthquakes generated by the creation of new fractures, whereas lower *b*-values are associated with the reactivation of pre-existing faults (Maxwell *et al.* 2009; Friberg *et al.* 2014; Benz *et al.* 2015). In the Bebedouro sequence, we believe that the low *b*-value is related to microseismicity generated by the reactivation of faults in pre-existing fractured zones within the basalt pack. At any rate, this deserves further investigation in the future.

4 ADDITIONAL GEOPHYSICAL STUDIES

For a more detailed study of the shallow structure, several geophysical surveys were performed; the geophysical techniques included seismic refraction, surface wave dispersion, VES, high-frequency receiver functions and TDEM. The high-frequency receiver functions and surface wave dispersions (Dias *et al.* 2011) indicated that the thickness of the Serra Geral basalt layer in Bebedouro ranged from 200 to 400 m. Additionally, the presence of low-velocity layers could be interpreted as potential fracture zones or altered layers within the basalt pack (Fig. 5). Fig. 6 shows a typical resistivity profile from a TDEM survey in Bebedouro. The VES and TDEM surveys indicated that the 60–70 m thick surface sandstone layer is generally composed of an upper dry layer (high resistivity, 70−100 Ωm) and a lower layer with a low resistivity (approximately 10 Ωm), which is interpreted as the shallow aquifer in the saturated sandstone. Under the surface layer, the surveys indicated the presence of a basalt layer (high resistivity, 70 Ωm) containing a very thin zone of low resistivity within the basalt pack (2−5 Ωm, basalt). Porsani *et al.* (2012), based on the high conductivity of the water in the fractures,

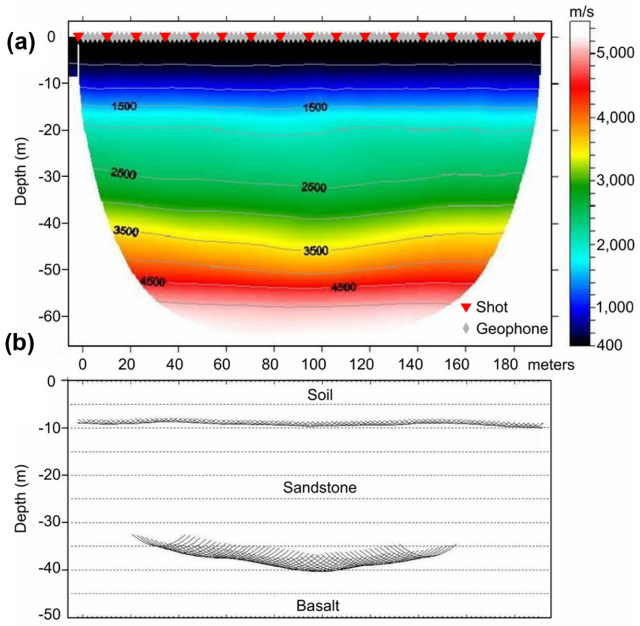

Figure 7. Results of the seismic refraction line near station BEB4A. (a) Tomographic inversion and (b) reciprocal method. The three layers correspond to soil, sandstone and basalt.

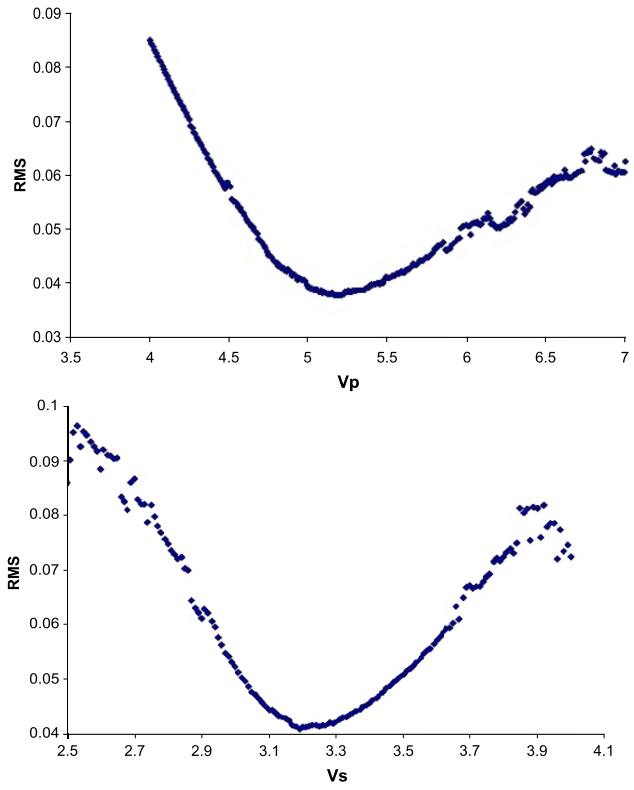

Figure 8. *Vp* and *Vs* in the basalt layer based on the minimal misfit (rms) in the basalt layer. (a) rms residual for the earthquake locations when *Vp* is varied. (b) rms residual for the earthquake locations when *Vs* is varied.

interpreted this thin zone as the confined fractured aquifer, which is in general agreement with the results obtained by Dias *et al*. (2011).

We performed shallow seismic refraction surveys in four areas near some seismographic stations (Fig. 3) using 96 14 Hz geophones at 2 m spacings and a hammer on a metal plate as the source. Fig. 6 shows the results of the seismic refraction line near station BEB4A. Moreover, we produced a smooth tomographic inversion (Fig. 7a) based on the Delta-t-V method using the Rayfract software (Gebrande & Miller 1985; Rohdewald 1999). Fig. 7(b) shows the result using the reciprocal method (Hagedoorn 1955). This analysis indicated the presence of three layers: a soil layer with a *P*-wave velocity of 400 ± 200 m s^{-1} and a thickness ranging from 1 to 12 m; a second layer (Bauru Group sandstone) with a *P*-wave velocity of 2700 ± 500 m s^{-1} and a third layer with a *P*-wave velocity of 5200 ± 500 m s^{-1}, corresponding to the Serra Geral basalt. The low velocity of the sandstone in this region suggests a high porosity and a high clay content (probably underconsolidated) sandstone (Han *et al.* 1986). As a result, we adopted the average layer thicknesses and average velocities obtained with the seismic refraction analysis to build an initial three-layer velocity model called 'mod0' (see Table 1).

5 NEW VELOCITY MODEL AND RELOCATION OF EARTHQUAKES

We selected the 526 events with the highest quality records, eight or more picks and an azimuthal gap of $\leq 180°$, to improve the initial *P*-wave velocity model, 'mod0'. We obtained a new 1-D velocity model, 'mod1', by minimizing the traveltime residuals (rms) through trial and error with 1000 runs of HYPOCENTRE locations. For this, we compute a repeated random sampling, such that the *P*- and *S*-wave velocities of each layer (soil, sandstone and basalt) were varied using the variance of the *P*-wave velocity model obtained with the seismic refraction analysis as sample limits and keeping the layers' thicknesses fixed (see Table 1 and Fig. 8).

The next step was to obtain an accurate and representative 1-D reference velocity model, or minimum 1-D model, using VELEST (Kissling 1988). This program is based on the coupled hypocentre–velocity model problem (Crosson 1976; Ellsworth 1977; Thurber

Table 1. Values of *Vp* (m s^{-1}), *Vs* (m s^{-1}) and *Vp*/*Vs* in the various models. The preliminary model is a simple two-layer model consisting of sandstone and basalt. The *a priori P*-wave velocity model,'mod0', the initial 1-D reference velocity model,'mod1' and the final 1-D velocity model,'mod2', consist of three layers. The best 1-D model was achieved using the methodology of a minimum 1-D velocity model from Kissling *et al*. (1994).

		Preliminary			Mod0			Mod1			Mod2		
Layer	Depth (m)	*Vp*	*Vs*	*Vp*/*Vs*	*Vp*	*Vs*	*Vp*/*Vs*	*Vp*	*Vs*	*Vp*/*Vs*	*Vp*	*Vs*	*Vp*/*Vs*
Soil	10	–	–	–	400	227	1.76	400	110	3.63	460	220	2.09
Sandstone	60	2200	1222	1.80	2700	1534	1.76	2700	1150	2.34	3020	1300	2.32
Basalt	500	5400	2777	1.80	5200	2955	1.76	5200	3200	1.62	5150	2710	1.90

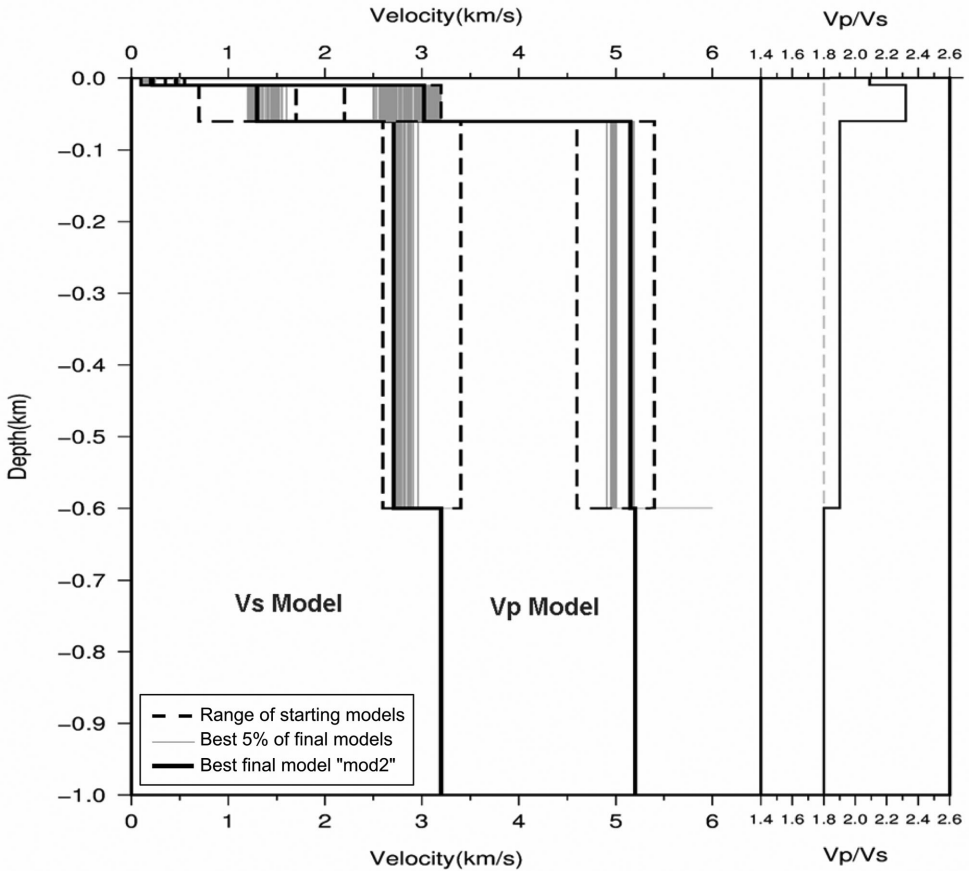

Figure 9. Final 1-D minimum velocity model,'mod2', for the *P* and *S* velocities and the *Vp*/*Vs* ratio. The dashed line indicates the range of the starting models; the grey lines indicate the best 5 per cent of the final models and the bold black line is the best final model with the lowest overall rms.

1977) and is used to simultaneously locate earthquakes and invert 1-D (layered) velocity models with station corrections. To measure the quality of each solution obtained by VELEST, the norm of the total traveltime differences, called rms residual or misfit, between the observed and the calculated traveltimes is estimated. Because this inverse problem is non-linear, the solution is obtained iteratively and strongly depends on the initial model and initial hypocentre locations. Thus, the inverse problem solution in VELEST is possibly non-unique, such that the procedure is to search for different solutions with minimal misfits (rmss) by varying the initial models and hypocentre locations within reasonable but large bounds (Kissling 1995). To do this, we selected 266 high-quality events from the previous subset of 526 events, including 1481 *P* and 1034 *S* phases, based on their number of observations ($\geq$8 picks), azimuthal gaps ($\leq$180°) and rms residuals ($\leq$0.05 s). Next, we computed 1000 runs with VELEST, varying the initial velocity models in a simultaneous inversion of hypocentral parameters (origin time, latitude, longitude and depth), velocity model (*Vp* and *Vs*) and station corrections. This is the standard procedure described by Kissling *et al*. (1994) and it allows *a posteriori* probability density function of the velocity model to be obtained. For the construction of the initial velocity models, we produced a suite of 1000 models that satisfied various measures of fit for the observations, assuming a thorough sampling of the combinations of velocity values for each layer within the normal distribution with the estimated parameters $N(\hat{\mu},\hat{\sigma})$ derived from the seismic refraction analysis and the results of 'mod1'. Fig. 9 shows the range of starting models used (parameters space). In the case of the *P* wave, the velocities parameters were as follows: 400 $\pm$ 200 m s^{-1} for soil, 2700 $\pm$ 500 m s^{-1} for sandstone and 5000 $\pm$ 400 m s^{-1} for the Serra Geral basalt. For the *S* wave, the following parameters were used: 100 $\pm$ 200 m s^{-1} for soil, 1100 $\pm$ 500 m s^{-1} for sandstone and 3000 $\pm$ 400 m s^{-1} for the basalt layer. Fig. 9 also displays the final 1-D velocity model obtained for both the *P* and *S* waves, as well as the *Vp*/*Vs* ratio. The grey lines in Fig. 9 show the best 5per cent of the models with the smallest *rms-misfit,* according to the given traveltimes data set. The spread of these lines indicates the distributions of the parameters being calibrated; in the case of the *P* velocity in the basalt, it is possible to identify two narrow regions of local minima. Thus, the model with the smallest *rms-misfit* for all earthquakes was accepted as the best possible estimate of the 1-D reference velocity model, or 1-D minimum model, 'mod2'.

The final velocities are consistent with velocities expected in this area, based on its geology and the seismic refraction surveys. Elevated *Vp*/*Vs* ratios of 1.9–2.3 were found in the basalts of the Serra Geral aquifer and the sedimentary rocks of the Bauru surface aquifer, respectively, as is expected of materials with open, fluid-filled pores/fractures (Mavko & Mukerji 1998; Daley *et al.* 2004).

To test the robustness and location stability of the final 1-D minimum model, we followed the procedure described by Kissling (1995), comparing the initial and final hypocentres. We created a suite of initial hypocentres by randomly shifting the locations obtained with the minimum 1-D model, and then relocated them using the minimum 1-D model. If the model proves to be robust, as

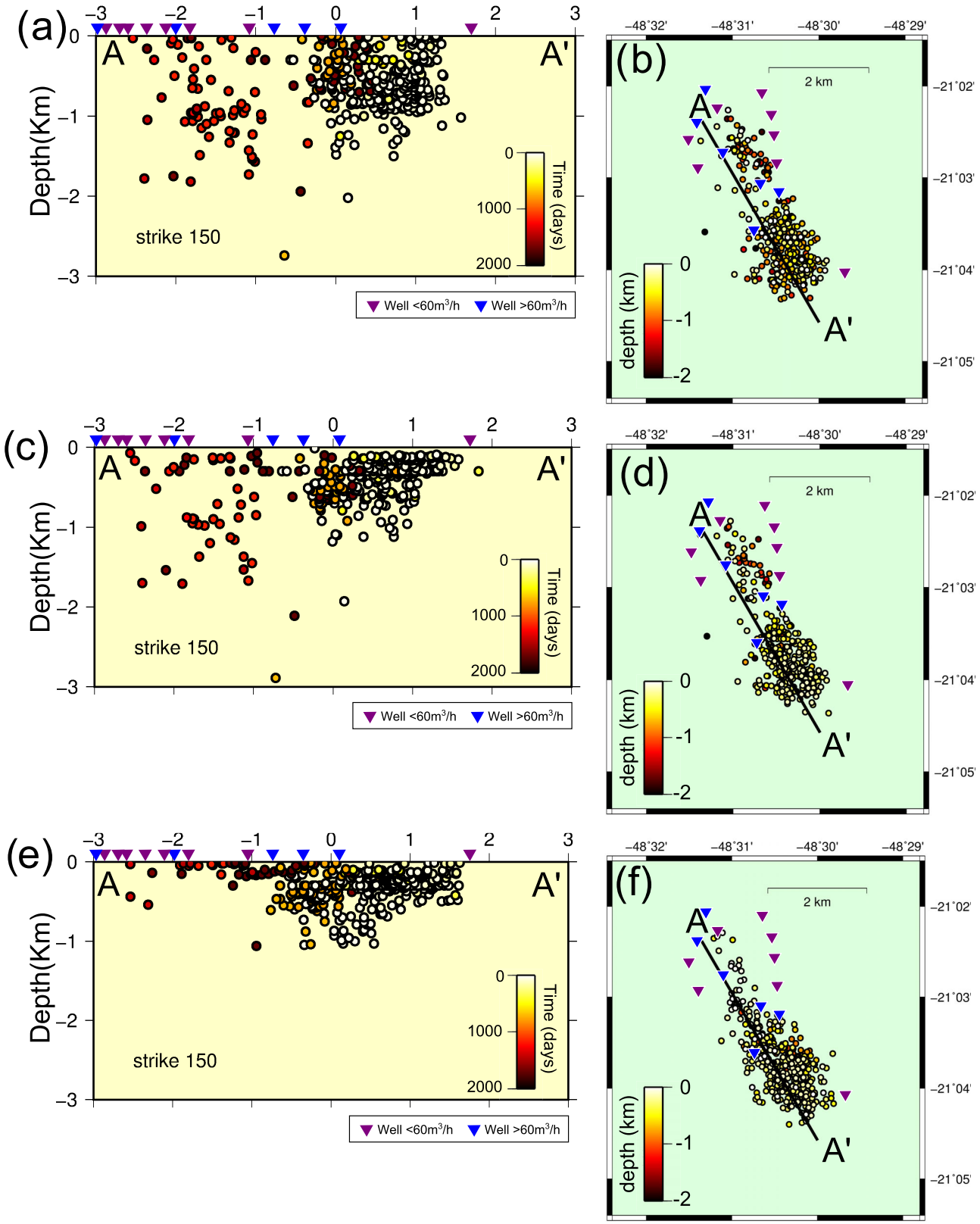

Figure 10. Hypocentral distribution of ~1000 best events (those with eight or more picks, an azimuthal gap of <180 and rms <0.05 s) based on the use of different models. (a) and (b) Initial model 'mod0', (c) and (d) model 'mod1' and (e) and (f) final model 'mod2'. In all of the right-hand panels (b), (d) and (f), the black line A–A′ in the map indicates the profile shown on the left.

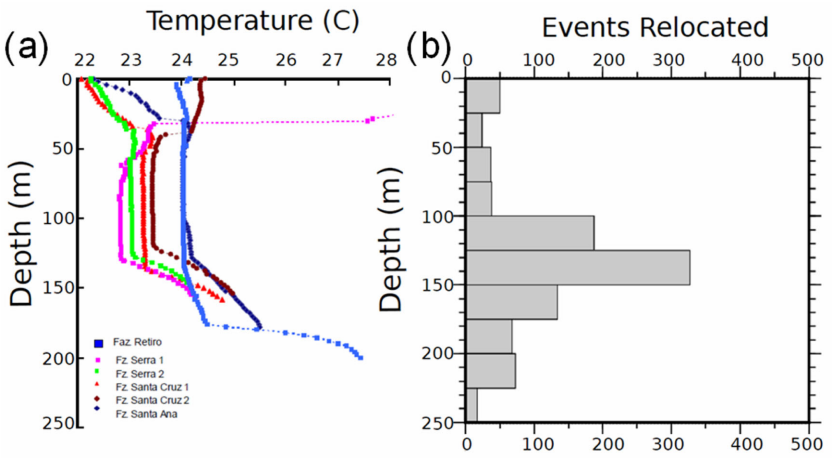

Figure 11. Correlation between the temperature profiles (left) and the distribution of the ∼1000 relocated event depths (right) using the new velocity model,'mod2'. Note zones with constant temperatures in all wells indicate water flowing down the well. The change from a constant temperature to temperature gradient (the 'kink' in the profile between 120 and 170 m) indicates the water entering the fractured aquifer. Part (a) is based on data published by Assumpção *et al*. (2010).

our results attest that it is (see Appendix), the relocated hypocentres should converge to their initial locations with negligible variations. Appendix summarizes the details of this stability test using the set of the 266 best events.

Fig. 10 shows the distribution of the HYPOCENTRE locations of ∼1000 events using the three different model scenarios. Figs 10(a) and (b) show the distribution using the initial model 'mod0'. The panel of Fig. 10(a) shows that the depth distribution varies widely (0–2 km), and most of the hypocentres are below the basalt layer; therefore, no correlation between the hypocentral depths and geology could be established. The panel of Fig. 10(b) shows the horizontal spread of the epicentres; they are concentrated in two regions and vary widely in depth. Figs 10(c) and (d) show the distribution using the model 'mod1'. The depth distribution of the hypocentres produced using 'mod1' (Fig. 10c) is within the narrower depth range of 0.1–0.6 km, and a significant number of hypocentres are concentrated at a depth of 300 m, which is the starting depth of the inversion process assigned to the hypocentres with poor depth resolutions. Figs 10(e) and (f) show a significant reduction of the uncertainties in the depths using the final model, 'mod2', with hypocentres mostly located at less than 500 m depths, concentrated between 100 and 200 m. This result indicates most of the events occurred within the basalt layer at the same depths as the fracture zones that receive extra water from the surface aquifer. Additionally, Fig. 10(e) suggests the possibility that there were changes in depth during the survey period and Fig. 10(f) shows the epicentres concentrated in a single region.

Fig. 11 shows the comparison of the temperature profiles of six wells in the Andes district (Fig. 11a, Assumpção *et al*. 2010) and a histogram of the hypocentral depths obtained with the final velocity model,'mod2' (Fig. 11b). In the empty (air-filled) parts of the wells, a variable temperature gradient is observed from the surface down to 30 m. A drastic change to a constant temperature can then be observed due to the inflow of water from the surface aquifer into the well. In those wells, the falling water could be clearly heard from the wellhead, suggesting the rapid influx of water from the upper aquifer into the well. A change from a constant temperature to a strong gradient, that is, a 'kink' in the temperature profile, is evident between 120 and 170 m. This kink indicates the entrance of cold water into the fractured aquifer in the basalt layers. Below the kink, the water is still and the temperature tends to resume a normal geothermal gradient. Assumpção *et al*. (2010) concluded that the additional water flowing into the fractured aquifer increases its pore pressure. The relocated events produced by the final model, 'mod2', are concentrated between the depths of 100 and 175 m (Fig. 11b), which coincide remarkably well with the depth of the fractured aquifer revealed by the temperature logging. This pattern would confirm that the seismic activity is positively correlated with an increase in pore pressure in the fractured aquifer due to the addition of water from the upper aquifer.

6 FOCAL MECHANISM AND RELATIVE LOCATION OF A CLUSTER

To better understand the nature of the Bebedouro seismicity, we selected and analysed a set of 19 well-recorded foreshocks and aftershocks that occurred between 2005 March 26 and 30, related to a magnitude 2.9 event, the largest of the whole series. In this area, the onset of the *P* and *S* arrivals is typically weak and emergent, which makes it difficult to pick accurate arrival times (Fig. 11). This is most likely due to one or more factors acting together to scatter the first arrivals: (1) a loss of energy in the low-velocity sandstone layer beneath the basalt, (2) diffusion that slightly delays the first arrivals (e.g. due to propagation in the fractured layer) and/or (3) the focal mechanism (*P* rays leaving the hypocentres at low angles from the nodal plane have weak amplitudes).

We used a method based on waveform cross-correlations and relative locations to better define the fault plane of the selected set. The relative precision of the hypocentres can be improved by obtaining more-accurate relative arrival-time readings using wave cross-correlations (Got *et al.* 1994; Waldhauser & Ellsworth 2000). The weak signals can be detected based on their consistent shapes and appearances in multiple seismograms or based on their similarity to a reference wavelet. We used the program CORR from the SEISAN software package (Havskov & Ottemöller 1999) to compute the cross-correlation between the same stations for all pairs of the 19 events and combine them in a cross-correlation matrix (Got *et al.* 1994). For the correlation analysis of the *P* waveform, we used the vertical components; for the *S* wave, we chose the horizontal component with the best record. We used a bandpass filter of 20–50 Hz to determine the correlation between all possible pairs

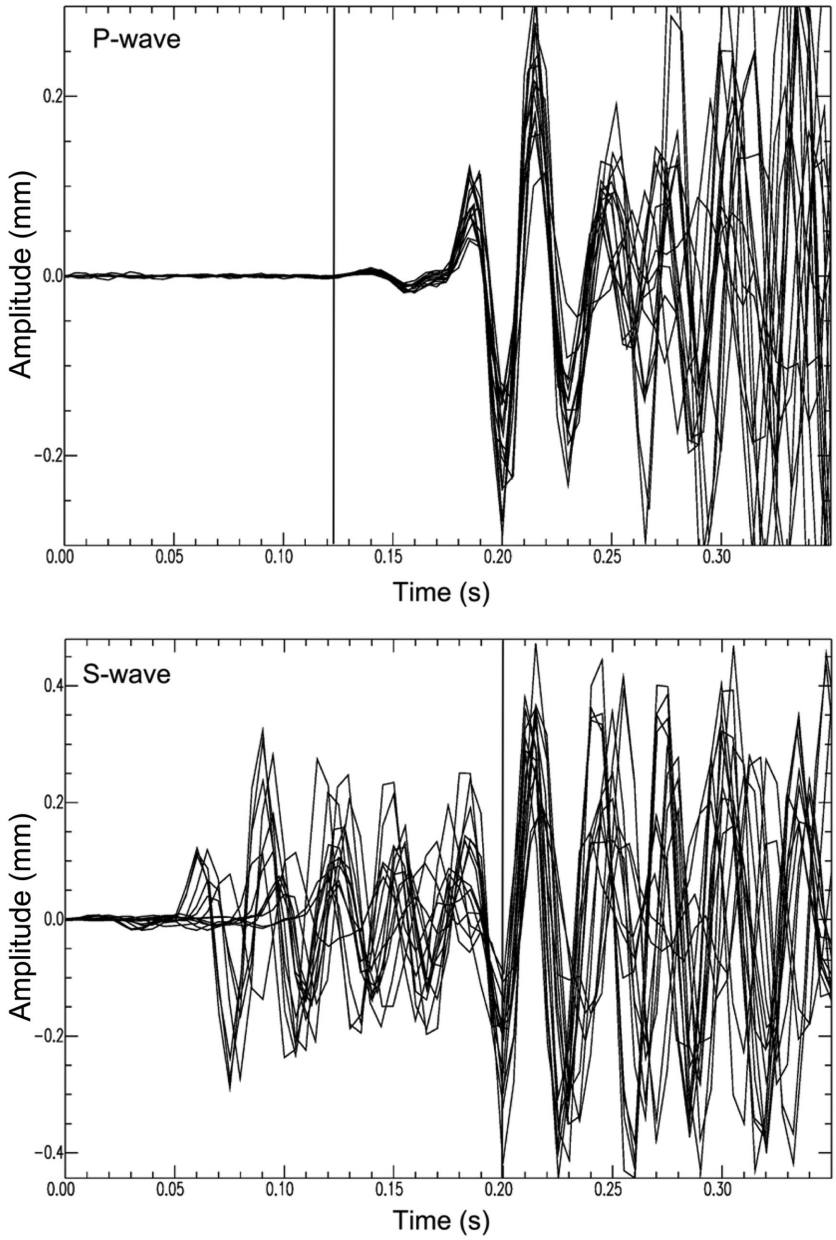

Figure 12. Stacked seismograms of the vertical component waveforms after they are cross-correlation aligned by *P* (top) and *S* waves (bottom) for the clustered earthquakes at station BEB1. Traces were bandpass filtered between 20 and 50 Hz.

of seismograms. Fig. 12 shows the stacked seismograms aligned by the *P* and *S* arrivals of the 19 correlated events recorded at station BEB1. The result is a high-precision set of arrival times that serves as an input for the relative relocation.

We combined the *P*- and *S*-wave differential times derived from the cross-correlations and used the HypoDD2 code to relocate the events (Waldhauser & Ellsworth 2000). For the relocation using a relative location method, we assumed that (1) the ray paths between the source region and a common station are similar along most of the ray path and (2) the separation between the hypocentres is small compared with the event-to-station distance (i.e. the events are clustered within a small area). Fig. 13 shows the relocated hypocentres. Profile A–A′ (left) shows the dip of the fault plane between the depths of 350 and 600 m. This plane is interpreted as a 500-m-long fault within the basalt layer pack, cutting along its entire length. A rupture of ∼500 m is consistent with the magnitude 2.9 (mb) of the main shock, according to the source parameter relationships of Nuttli (1983). The hypocentres define a best-fitting plane with a strike of 260° and a dip of 40° to the NE.

We also calculated a composite fault-plane solution for the 19 clustered events using *P*-wave first-motion polarities. Fig. 14 shows the polarity distributions and two nodal planes. The solid line shows the best fault-plane solution (normal fault with NS *T*-axis), with a 247° strike, a dip of 50° to the NE and −40° of rake. This nodal plane solution is consistent with the fault plane fitted to the relocated hypocentres (Fig. 13).

7 DISCUSSION AND CONCLUSIONS

Previous works conducted in Bebedouro (Assumpção *et al*. 2007, 2010; Porsani *et al.* 2012) indicated that the seismic events occurred due to increased pore pressures in the fractured aquifer. In

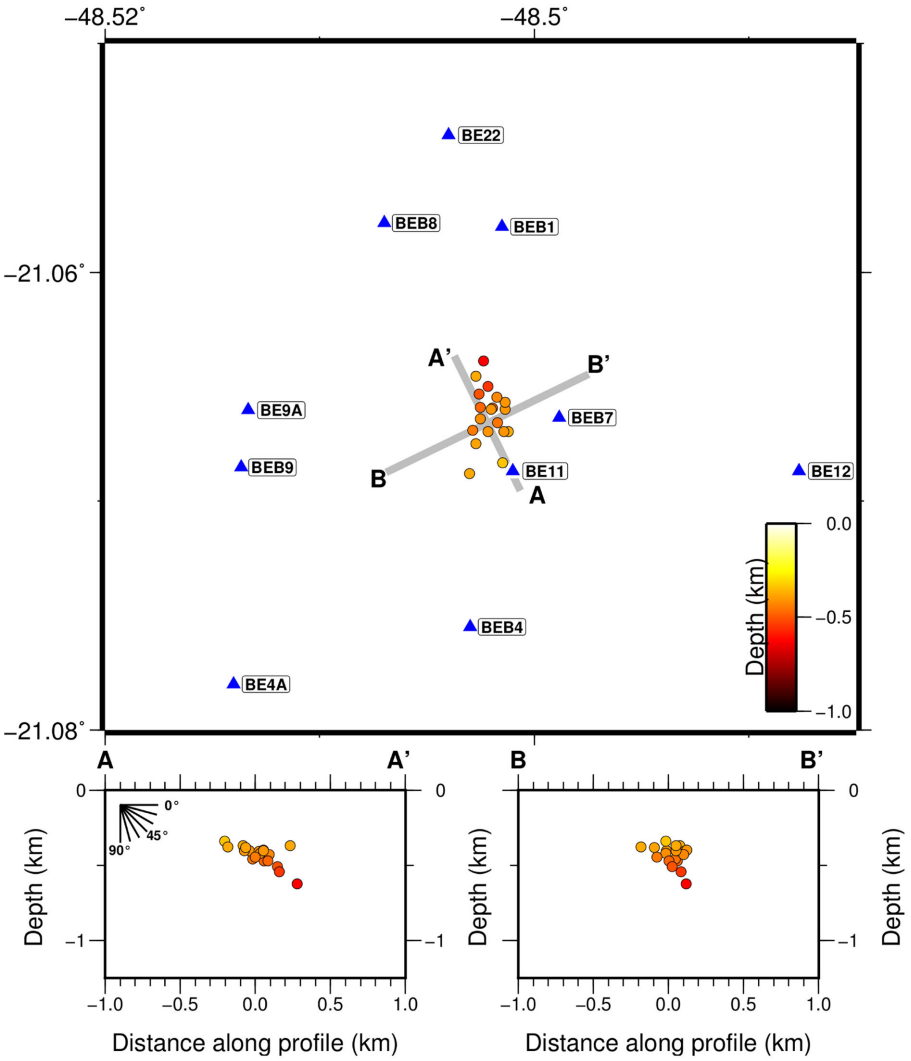

Figure 13. Relocation of the 19 highly correlated events based on the *P*- and *S*-wave cross-correlated differential traveltimes. Top panel: map view. Lower left: cross-section A–A′, which is drawn along the dip direction. Lower right: cross-section B–B′, drawn parallel to the strike. The plane best fitted to the cluster strikes at 260° and dips at 40° to the NE.

those studies, the proposed triggering mechanism was that most wells in this area act as conduits for moving water from an upper aquifer down to the fractured aquifer, thereby increasing the water pressure. The weight of the water column in the well causes changes in pore pressure and effective stress in the fractured zones (assumed to be previously under critical stress) within the basalt pack, eventually generating creep or rupture along the faults. These conclusions agree with some examples of wells injecting water via gravity, which increases the fluid pressure and induces earthquakes (Barnhart *et al.* 2014; Rubinstein *et al.* 2014). However, in the case of Bebedouro, the large depth uncertainty made it difficult to confirm this hypothesis because it could not be established that the earthquakes nucleated inside the basalt pack.

Davis & Frohlich (1993) developed three primary criteria to determine if seismicity is induced by fluid injection activities: (1) coincident locations, (2) coincident timings and (3) adequate fluid pressures. Figs 9(e) and (f) suggest that using the improved 1-D velocity model, we accurately relocated the events and demonstrated that most of them occur between the depths of 100 and 175 m, that is, mostly within the basalt layer, at the same depths as the fracture zones that receive extra water from the surface aquifer. The adequate pressures would have been introduced to cause the earthquakes by disturbances (pore pressure increases) of the geological stresses in pre-existing critically stressed fracture zones within the basalt layer, presumably by reducing the effective normal stress (McGarr *et al.* 2002; Friberg *et al.* 2014). These findings suggest that the three criteria were achieved and thus support the hypothesis of seismicity triggered by hydraulic stimulation in deep-water wells (drilled in early 2003 and 2006) via a gravity feed.

Fig. 2 shows additional evidence that supports this hypothesis: the timing of the earthquake activity peaks approximately two months after the annual peak in rainfall, due to a delay in the diffusion of the pore pressure increase in the fracture zone; when the pore pressure is reduced by pumping, the activity ceases. This process will likely persist as long as pore pressures changes in the hypocentral region continue to exist, as described by Ellsworth (2013). However, the observed trend of the decreasing amplitudes of the earthquake peaks (as suggested by Fig. 2) may indicate that the available stresses were eventually relieved after approximately seven years.

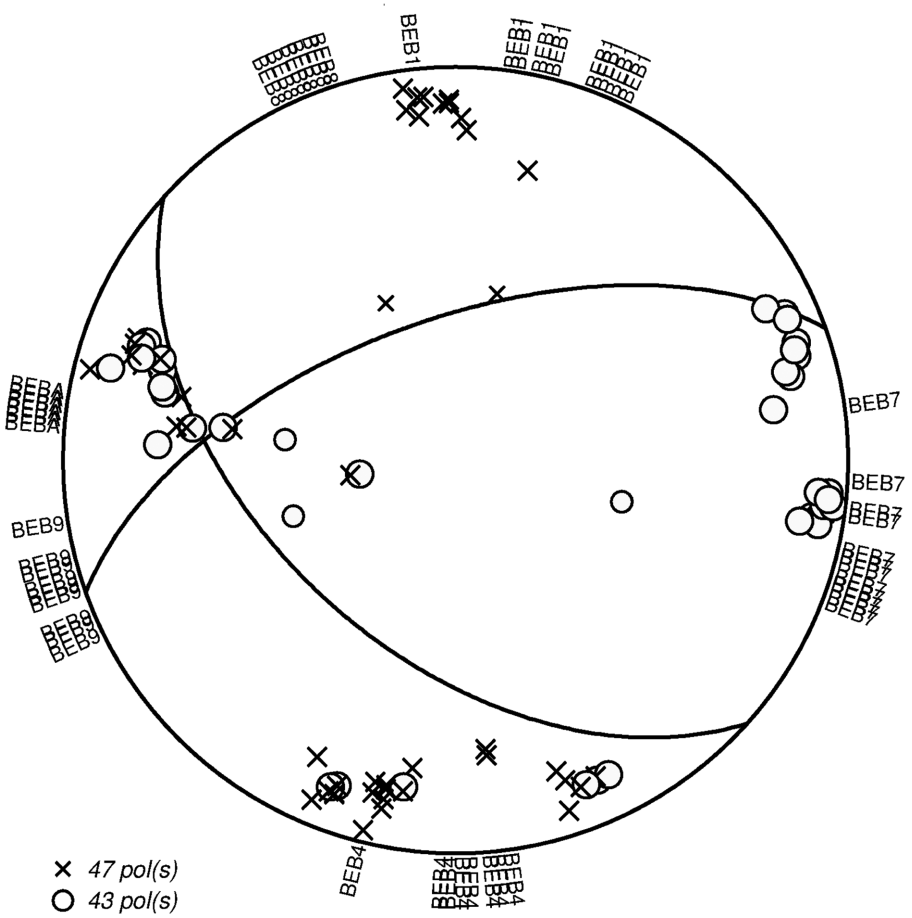

Figure 14. Composite focal mechanism solution: *P*-wave first-motion polarities: upward (x) and downward (circles). Solid lines are the nodal planes based on the *P*-wave polarities.

The use of cross-correlation and relative hypocentral locations allowed a clear determination of the fault-plane solution of one of the largest events: a normal fault striking WSW-ENE, with a dip to the north and a NNW-SSE extension (*T*-axis). The analysis of several focal mechanisms in the southern Minas Gerais state (a few hundred kilometres NE of Bebedouro, in the same regional seismic zone) indicated that the regional stress consists of E-W compression and N-S extension (Assumpção 1998; Assumpção *et al.* 2016). The normal faulting observed in Bebedouro is consistent with this regional stress.

Our findings improve our understanding of the mechanics of the seismicity triggered by water wells in the Paraná Basin and may contribute to future environmental policies regarding underground water exploration. However, to potentially reduce the seismic activity and advance risk mitigation, more work is needed to better understand the atypical earthquake sequences caused by gravity feeds, like that in Bebedouro. More information about the geological conditions, the state of the stress and especially the industrial activity of the wells would be necessary (Petersen *et al*. 2016) and would require collaboration between scientists and well owners. Although the inversion procedure used to obtain the best 1-D model was standard, the use of shallow geophysical surveys to constrain some of the parameters in the initial models proved to be very important.

The Bebedouro sequence was unusual in its persisting yearly cycles. However, a large number of wells are drilled every year in the Paraná Basin, and many small, short-lived earthquake sequences also occur. It could be that seismicity induced by drilling water wells is more common but other cases may have gone unnoticed due to a lack of detailed studies.

ACKNOWLEDGEMENTS

We thank the people of the Andes district for help during the field work. We benefited from discussions with several colleagues, particularly Tereza H. Yamabe, Fabio Luiz Dias, Emerson Almeida, Igor Almeida and Cassiano Bortolozo. The first stations were installed by Luis Galhardo, Dennis Schramm and CéliaFernandes, for which we are thankful. We thank the PEC-PG and CNPq postgraduate scholarship awarded to Gabriel Dicelis. This research was supported by the FAPESP grant nos 2014/09455-3 and 2007/04325-0. We thank Editor Ingo Grevemeyer, and two anonymous reviewers for their comments and suggestions.

REFERENCES

Agurto, H., Rietbrock, A., Barrientos, S., Bataille, K. & Legrand, D., 2012. Seismo-tectonic structure of the Aysén Region, Southern Chile, inferred from the 2007 *M*w=6.2 Aysén earthquake sequence, *Geophys. J. Int.,* **190,** 116–130.

Assumpção, M., 1983. A regional magnitude scale for Brazil, *Bull. seism. Soc. Am.,* **73,** 237–246.

Assumpção, M., 1998. Focal mechanisms of small earthquakes in SE Brazilian shield: a test of stress models of the South American plate, *Geophys. J. Int.,* **133,** 490–498.

Assumpção, M. & Sacek, V., 2013. Intra-plate seismicity and flexural stresses in Central Brazil, *Geophys. Res. Lett.,* **40,** 487–491.

Assumpção, M., Schimmel, M., Escalante, C., Barbora, J.R., Rocha, M & Barros, L., 2004. Intraplate seismicity in SE Brazil: stress concentration in lithospheric thin spots, *Geophys. J. Int.,* **159,** 390–399.

Assumpção, M., Barbosa, J.R., Lopes, A., Balancin, L. & Yamabe, T., 2007. Seismic activity induced by water wells, Paraná Basin, Brazil, in *10th International Congress of the Brazilian Geophysical Society & EXPOGEF 2007,* Rio de Janeiro, Brazil, November 19–22, Extended Abstract, pp. 835–839, doi:10.1190/sbgf2007-162.

Assumpção, M., Yamabe, T.H., Barbosa, J.R., Hamza, V., Lopes, A.E.V., Balancin, L. & Bianchi, M.B., 2010. Seismic activity triggered by water wells in the Paraná Basin, Brazil, *Water Resour. Res.,* **46,** W07527, doi:10.1029/2009WR008048.

Assumpção, M. *et al.*, 2014. Intraplate seismicity in Brazil, in *Intraplate Earthquakes*, chap. 3, ed. Talwani, P., Cambridge Univ. Press.

Assumpção, M., Dias, F.L., Zevallos, I. & Naliboff, J.B., 2016. Intraplate stress field in South America from earthquake focal mechanisms, *J. South Amer. Earth Sci.,* **71,** 278–295.

Bachmann, C.E., Wiemer, S., Woessner, J. & Hainzl, S., 2011. Statistical analysis of the induced Basel 2006 earthquake sequence: introducing a probability-based monitoring approach for enhanced geothermal systems, *Geophys. J. Int.,* **186**(2), 793–807.

Bachman, C.E., Wiemer, S., Goertz-Allmann, B.P. & Woessner, J., 2012. Influence of pore-pressure on the event-size distribution of induced earthquake, *Geophys. Res. Lett.,* **39,** L09302, doi:10.1029/2012GL051480.

Barnhart, W., Benz, H., Hayes, G.P., Rubinstein, J.L. & Bergman, E., 2014. Seismological and geodetic constraints on the 2011 Mw 5.3 Trinidad, Colorado earthquake and induced deformation in the Raton Basin, *J. geophys. Res.,* **119,** doi:10.1002/2014JB011227.

Benz, H.M., McMahon, N.D., Aster, R.C., McNamara, D.E. & Harris, D.B., 2015. Hundreds of earthquakes per day: the 2014 Guthrie, Oklahoma, earthquake sequence, *Seismol. Res. Lett.,* **86**(5), 1318–1325.

Berrocal, J., Assumpção, M., Antezana, R., Dias Neto, C.M., Ortega, R., França, H. & Veloso, J., 1984. *Sismicidade do Brasil,* IAG-USP/CNEN, São Paulo, p. 320.

Cox, R.T., 1991. Possible triggering of earthquakes by underground waste disposal in the El Dorado, Arkansas area, *Seismol. Res. Lett.,* **62**(2), 113–122.

Crosson, R.S., 1976. Crustal structure modeling of earthquake data: 1. Simultaneous least squares estimation of hypocentre and velocity parameters, *J. geophys. Res.,* **81,** 3036–3046.

Daley, T.M., Majer, E.L. & Peterson, J.E., 2004. Crosswell seismic imaging in a contaminated basalt aquifer, *Geophysics,* **69**(1), 16–24.

Davis, S. & Frohlich, C. 1993. Did (Or will) fluid injection cause earthquakes?—criteria for a rational assessment, *Seismol. Res. Lett.,* **64**(3–4), 207–224.

Davis, S.D., Nyffenegger, P.A. & Frohlich, C., 1995. The 9 April 1993 earthquake in south-central Texas: was it induced by fluid withdrawal?, *Bull. seism. Soc. Am.,* **85,** 1888–1895.

Dias, F., Assumpção, M., Barbosa, J. & Prado, R., 2011. *Study of Basalt Layer in Bebedouro, Paraná Basin, with Receiver Function. Active Seismic Triggered by Depth Wells Implications,* Simpósio Nacional de Estudos Tectônicos.

Deichmann, N. & Giardini, D., 2009. Earthquakes induced by the stimulation of an enhanced geothermal system below Basel (Switzerland), *Seismol. Res. Lett.,* **80**(5), 784–798.

Eck, T.V., Goutbeek, F. & Haak, H., 2006. Seismic hazard due to small-magnitude, shallow-source, induced earthquakes in the Netherlands, *Eng. Geol.,* **87,** 105–121.

Ellsworth, W.L., 1977. Three-dimensional structure of the crust and mantle beneath the island of Hawaii, *PhD thesis*, MIT, Massachussetts, USA.

Ellsworth, W.L., 2013. Injection-induced earthquakes, *Science,* **341,** doi:10.1126/science.1225942.

Farrell, J., Husen, S. & Smith, R.B., 2009. Earthquake swarm and b-value characterization of the Yellowstone volcanic-tectonic system, *J. Volc. Geotherm. Res.,* **188,** 260–276.

Friberg, P.A., Besana-Ostman, G.M. & Dricker, I., 2014. Characterization of an earthquake sequence triggered by hydraulic fracturing in Harrison County, Ohio, *Seismol. Res. Lett.,* **85,** 1295–1307.

Frohlich, C., 2012. Two-year survey comparing earthquake activity and injection-well locations in the Barnett Shale, Texas, *Proc. Natl. Acad. Sci. USA,* **109**(35), 13 934–13 938.

Gebrande, H. & Miller, H., 1985. Refraktionsseismik, in *Angewandte Geowissenschaften II*, pp. 226–260, ed. Bender, F., Ferdinand Enke, Stuttgart.

Got, J., Fréchet, J. & Klein, F.W., 1994. Deep fault plane geometry inferred from multiplet relative relocation beneath the south flank of Kilauea, *J. geophys. Res.,* **99,** 15 375–15 386.

Gutenberg, B. & Richter, C.F., 1942. Earthquake magnitude intensity, energy, and acceleration, *Bull. seism. Soc. Am.,* **32,** 163–191.

Hagedoorn, J., 1955. Templates for fitting smooth velocity functions to seismic refraction and reflection data, *Geophys. Prospect.,* **3,** 325–338.

Han, D., Nur, A. & Morgan, D., 1986. Effects of porosity and clay content on wave velocities in sandstones, *Geophysics,* **51**(11), 2093–2107.

Havskov, J. & Ottemöller, L., 1999. SeisAn Earthquake analysis software, *Seismol. Res. Lett.,* **70**. Available at: http://www.seismosoc.org/publications/SRL/SRL_70/srl_70-5_es.html

Holland, A.A., 2013. Earthquakes triggered by hydraulic fracturing in South-Central Oklahoma, *Bull. seismol. Soc. Am.,* **103,** 1784–1792.

Horton, S., 2012. Disposal of hydrofracking-waste fluid by injection into subsurface aquifers triggers earthquake swarm in central Arkansas with potential for damaging earthquake, *Seismol. Res. Lett.,* **83**(2), 250–260.

Hubbert, M.K. & Rubey, W.W., 1959. Role of fluid pressure in mechanics of overthrust faulting I. Mechanics of fluid-filled porous solids and its application to overthrust faulting, *Bull. geol. Soc. Am.,* **70**(2), 115–166.

Husen, S., Kissling, E., Flueh, E. & Asch, G., 1999. Accurate hypocentre determination in the seismogenic zone of the subducting Nazca plate in northern Chile using a combined on-/offshore network, *Geophys. J. Int.,* **138,** 687–701.

Keranen, K.M., Weingarten, M., Abers, G.A., Bekins, B.A. & Ge, S., 2014. Sharp increase in central Oklahoma seismicity since 2008 induced by massive wastewater injection, *Science,* **345,** 448–451.

Kim, W.Y., 2013. Induced seismicity associated with a fluid injection into deep well in Youngstown, Ohio, *J. geophys. Res.,* **118,** 3506–3518.

Kissling, E., 1988. Geotomography with local earthquake data, *Rev. Geophys.,* **26**(4), doi:10.1029/RG026i004p00659.

Kissling, E., 1995. *Program VELEST User's Guide—Short Introduction,* Second draft version, Institute of Geophysics, ETH Zurich.

Kissling, E., Ellsworth, W., Eberhart-Phillips, D. & Kradolfer, U., 1994. Initial reference model in local earthquake tomography, *J. geophys. Res.,* **99**(B10), 19 635–19 646.

Lee, W.H.K. & Lahr, J.C., 1975. HYPO71: a computer program for determining hypocentre, magnitude, and first motion pattern of local earthquakes. Open-File Rep., United States Department of the Interior Geological Survey, National Center for Earthquake Research, Menlo Park, California, 75-311, p. 64.

Lienert, B.R.E. & Havskov, J., 1995. A computer program for locating earthquakes both locally and globally, *Seismol. Res. Lett.,* **66,** 26–36.

Lienert, B.R., Berg, E. & Frazer, L.N., 1986. HYPOCENTER: an earthquake location method using centered, scaled, and adaptively damped least squares, *Bull. seism. Soc. Am.,* **76,** 771–783.

Maxwell, S.C. *et al.* 2009. Fault activation during hydraulic fracturing, in *SEG Technical Program Expanded Abstracts*, pp. 1552–1556, doi:10.1190/1.3255145.

McGarr, A., Simpson, D. & Seeber, L., 2002. Case histories of induced and triggered seismicity, in *International Handbook of Earthquake and Engineering Seismology, Part A,* International Geophysics, Vol. 81, Part A,

pp. 647–661, eds Lee, W.H.K., Kanamori, H., Jennings, P.C. & Kisslinger, C., Academic Press.

Mavko, G. & Mukerji, T., 1998. Bounds on low-frequency seismic velocities in partially saturated rocks, *Geophysics,* **63,** 918–924.

Milani, E.J., 2004. Comentários sobre a origem e a evolução tectônica da Bacia do Paranã, *Geologia do continente sul-americano: evolução da obra de Fernando Flávio Marques de Almeida,* São Paulo, Beca, pp. 265–279.

Milani, E.J., Melo, J.H.G., Souza, P.A., Fernandes, L.A. & França, A.B., 2007. Bacia do Paraná. Cartas Estratigráficas, *Boletim de Geociências da Petrobrás,* **15**(2), 265–287.

Nuttli, O., 1983. Average seismic source parameter relations for midplate earthquakes, *Bull seism. Soc. Am.,* **73,** 519–535.

Oliveira, I., Assumpção, M. & Agurto-Detzel, H. 2014. Variations of parameter b in SE Brazil from local earthquakes, *Earth Sci. Res. J.,* **18** (Special Issue).

Petersen, M.D. *et al.*, 1996. Seismic-hazard forecast for 2016 including induced and natural earthquakes in the Central and Eastern United States, *Seismol. Res. Lett.,* **87,** doi:10.1785/0220160072.

Porsani, J.L., Almeida, E.R., Bortolozo, C. & Monteiro, F., 2012. TDEM survey in an area of seismicity induced by water wells in Paraná sedimentary basin, Northern São Paulo State, Brazil, *J. appl. Geophys.,* **82,** 75–83.

Raleigh, C.B., Healy, J.H. & Bredehoeft, J.D., 1976. An experiment in earthquake control at Rangely, Colorado, *Science,* **191**(4233), 1230–1237.

Rohdewald, S.R., 1999. *Rayfract Manual,* Intelligent Resources Inc. Retrieved from http://rayfract.com/help/manual.pdf, last accessed 19 May 2016.

Rubinstein, L. & Mahani, A. 2015. Myths and facts on wastewater injection, hydraulic fracturing, enhanced oil recovery, and induced seismicity, *Seismol. Res. Lett.,* **86**(4), doi:10.1785/0220150067.

Rubinstein, J.L., Ellsworth, W.L., McGarr, A. & Benz, H.M., 2014. The 2001-present induced earthquake sequence in the Raton Basin of northern New Mexico and southern Colorado, *Bull. seism. Soc. Am.,* **104**(5), 2162–2181.

Schorlemmer, D., Wiemer, S. & Wyss, M., 2005. Variations in earthquake-size distribution across different stress regimes, *Nature,* **437,** 539–542.

Seeber, L., Armbruster, J.G. & Kim, W.-Y., 2004. A fluid-injection triggered earthquake sequence in Ashtabula, Ohio—implications for seismogenesis in stable continental regions, *Bull. seism. Soc. Am.,* **94**(1), 76–87.

Shapiro, S.A., Huenges, E. & Borm, G., 1997. Estimating the crust permeability from fluid-injection-induced seismic emission at the KTBsite, *Geophys. J. Int.,* **131**(2), F15–F18.

Shapiro, S.A. & Dinske, C., 2009. Fluid-induced seismicity: pressure diffusion and hydraulic fracturing, *Geophys. Prospect.,* **57**(2007), 301–310.

Shapiro, S.A., Rothert, E., Rath, V. & Rindschwentner, J., 2002. Characterization of fluid transport properties of reservoirs using induced microseismicity, *Geophysics,* **67**(1), 212–220.

Simpson, D. & Narasimhan, T., 1990. Inhomogenities in rock properties and their influence on reservoir induced seismicity, GerlandsBeitr, *Geophysics,* **99,** 205–220

Sumy, D.F., Cochran, E.S., Keranen, K.M., Wei, M. & Abers, G.A., 2014. Observations of static Coulomb stress triggering of the November 2011 M5.7 Oklahoma earthquake sequence, *J. geophys. Res.,* **119,** 1904–1923.

Thurber, C.H., 1977. Earth structure and earhtquake locations in the Coyote Lake area, central California, *PhD thesis*, MIT, Massachussetts, USA.

Turner, S., Regelous, M., Kelley, C., Hawkesworth, C. & Mantovani, M., 1994. Magnetism and continental break-up in the South Atlantic: Ar-Argeocronology, *Earth planet. Sci. Lett.,* **121,** 333–348.

Waldhauser, F., 2001. HypoDD: a computer program to compute double-difference earthquake locations, Open-File Rep., U.S. Geol. Surv., 01–113.

Waldhauser, F. & Ellsworth, W., 2000. A double difference earthquake location algorithm: method and application to the northern Hayward fault, California, *Bull. seism. Soc. Am.,* **90,** 1353–1368.

Wiemer, S. & Wyss, M., 2000. Minimum magnitude of complete reporting in earthquake catalogs: examples from Alaska, the western United States, and Japan, *Bull. seism. Soc. Am.,* **90,** 859–869.

Zoback, M., 2012. Managing the seismic risk posed by wastewater disposal, *Earth Mag.,* **57,** 38–43.

APPENDIX: TESTING THE ROBUSTNESS OF THE VELOCITY MODEL

To test the robustness and location stabilities of our final model, we computed a systematic test of 100 runs of VELEST, randomly shifting the initial hypocentral locations obtained using ‘mod2’ by as much as ±1.5 km horizontally and ±0.15 km vertically, while overdamping the velocity and station corrections. If the results of this test show a robust 1-D velocity model, we should obtain negligible variations of the 1-D model and the shifted hypocentres should be relocated back to their original positions (Kissling 1995; Husen *et al.* 1999; Agurto *et al.* 2012). As expected, most of the hypocentres were relocated to near their original positions. The relocated latitudes and longitudes have standard deviations of ±72 m and ±106 m, respectively (Figs A1b and c). The average σ of the depth (Fig. A1a) is ±76 m, which, despite being a relatively large standard deviation that corresponds to the 90 per cent confidence interval, is ∼10 times better than those of ‘mod0’ and ‘mod1’.

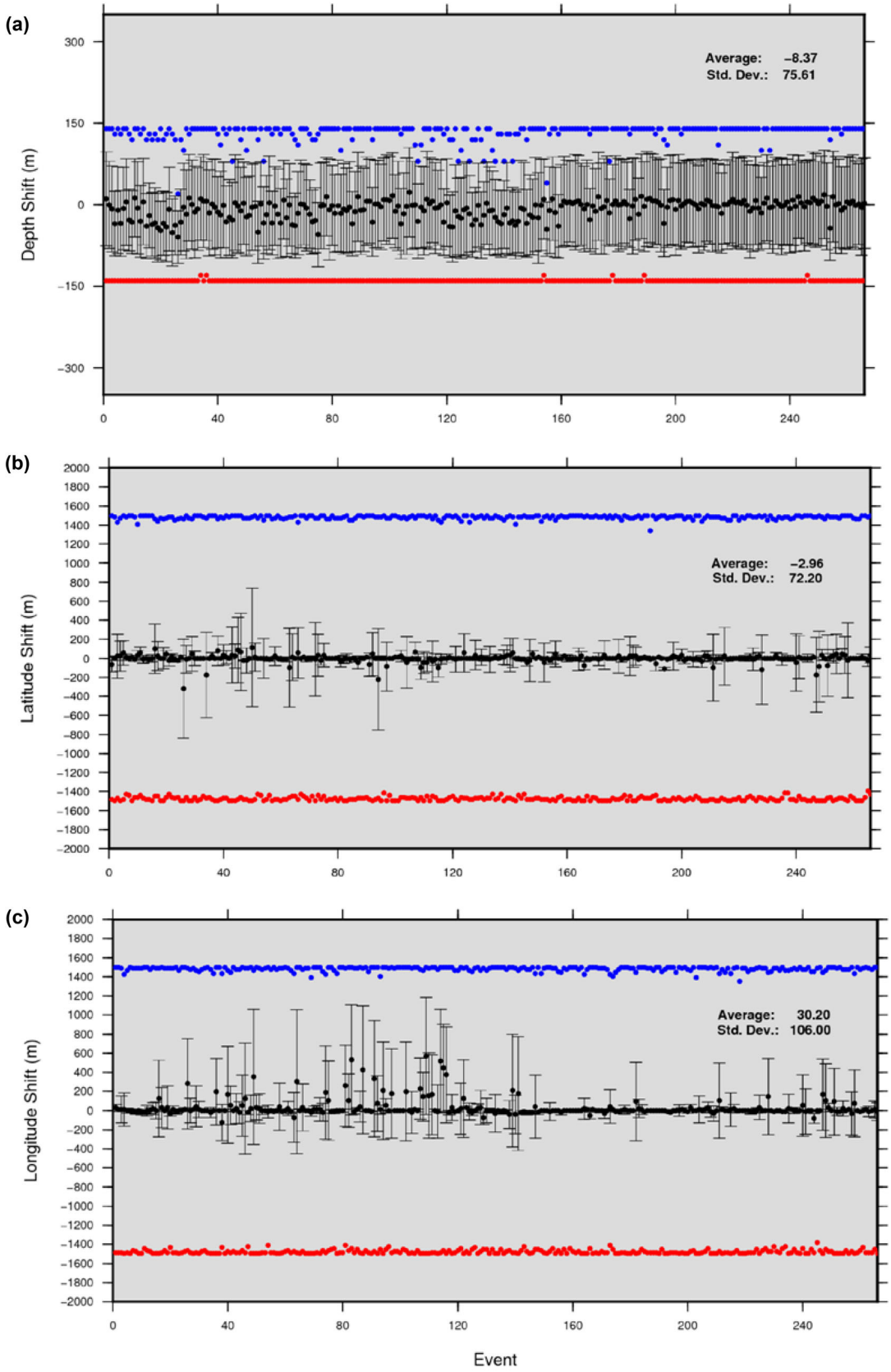

Figure A1. Hypocentre stability test. Black dots and errors bars are the average relocations and standard deviations for each event after a series of tests consisting of randomly shifting the latitude, longitude and depth of the original (initial) hypocentres. The blue and red dots show the maximum positive and minimum negative random shifts, respectively. (a) Test in depth. (b) Test in latitude and (c) Test in longitude.